JOURNAL OF GEOPHYSICAL RESEARCH, VOL. 113, C11018, doi:10.1029/2008JC004875, 2008

On the origins of the variability of the Malvinas Current in a global, eddy-permitting numerical simulation

Antonio F. H. Fetter[1] and Ricardo P. Matano[1]

Received 17 April 2008; revised 5 September 2008; accepted 16 September 2008; published 21 November 2008.

[1] This article investigates the origins of the variability of the Malvinas Current (MC) transport using the results of an eddy-permitting ocean general circulation model. First, the dynamical links between the variabilities of the MC and the Antarctic Circumpolar Current (ACC) transports at the Drake Passage are established. Time series analyses indicate that the connection between the transport variations of the ACC and the MC is masked by high-frequency oscillations. Although a substantial portion of this high-frequency variability is produced and dissipated locally, there are also anomalies that propagate between those regions. The most conspicuous of these signals has an average speed of $\sim$6–7 cm s^{-1} and a period of $\sim$150 days. Second, the contribution of the wind forcing to the variability of the ACC and the MC is determined from Principal Estimator Patterns analysis. The analysis indicates that the variance of the transport of both currents is more directly related to the variability of the wind stress than to the wind stress curl. The transport variability is particularly sensitive to zonal wind stress anomalies in the latitudinal range of the Drake Passage that extends farther north over the South Indian Ocean. A rather counterintuitive result of our analysis is that the wind stress forcing over the South Atlantic Ocean is unimportant to the variability of the MC transport.

Citation: Fetter, A. F. H., and R. P. Matano (2008), On the origins of the variability of the Malvinas Current in a global, eddy-permitting numerical simulation, *J. Geophys. Res.*, *113*, C11018, doi:10.1029/2008JC004875.

1. Introduction

[2] The Malvinas Current (MC) branches from the Antarctic Circumpolar Current (ACC) at the Drake Passage and flows equatorward along the continental slope of South America until it meets the poleward flow of the Brazil Current (BC) at $\sim$38°S, where it forms the Brazil-Malvinas Confluence (hereafter called the Confluence). It has been posited that the intense mesoscale variability of this region, which influences the regional marine ecosystems and climate [*Froneman et al.*, 1997; *Brandini et al.*, 2000], is driven partially by variations of the MC transport. Several studies have tried to understand the origins of the variability of the MC, particularly the linkages between the variations of the MC transport, the ACC transport and the Southern Ocean's winds. These studies, however, have produced ambiguous results that are characterized by sharp discrepancies between the conclusions derived from observations and models. The former studies state that there is a low correlation between the fluctuations of the ACC and the MC transports [*Matano et al.*, 1993; *Garzoli and Giulivi*, 1994; *Vivier et al.*, 2001], and the latter suggest just the opposite [*Smith et al.*, 1994; *Gan et al.*, 1998; *Wainer et al.*, 2000]. In this article, we seek to establish the links between the transport variations of the MC and the ACC at the Drake Passage, and their respective dependences on the wind forcing over the entire Southern Ocean using the results of an eddy-permitting global ocean model. We argue that the discrepancies of previous studies follow from the fact that they did not resolve the same spatial and temporal scales. Observations were limited by the shortness of the data record, which only allowed resolving fluctuations of relatively short period, while models were handicapped by the lack of spatial resolution, which did not allow the development of the energetic high-frequency oscillations that characterize the observational time series. In particular, models were hampered by their inability to represent the small-scale topographic features that frequently short circuit the large-scale circulation and that lead models to overestimate the connectivity among different portions of the Southern Ocean. The choice of the Drake Passage as a reference point for our study was motivated by its proximity to the MC and the fact that it is a natural choke point of the ACC and hence a good proxy of its overall variability.

[3] This article is organized as follows: after this introduction, in section 2, we make a brief description of the numerical simulation used in the analysis. In section 3, we present a kinematic description of the ACC and of the MC, and we investigate the dynamical mechanisms that link the ACC to the MC and the responses of these two currents to variations of the wind stress and wind stress curl over the Southern Ocean.

2. Model Description

[4] The numerical simulation used here was performed by R. Tokmakian using the Parallel Ocean Circulation Model

[1]College of Oceanic and Atmospheric Sciences, Oregon State University, Corvallis, Oregon, USA.

0148-0227/08/2008JC004875$09.00

(POCM) [*Tokmakian and Challenor*, 1999]. The model equations were discretized to a Mercator grid with an average horizontal grid spacing of 1/4° and 20 vertical levels. The bottom topography of the model was derived from the 1/12° ETOPO5 data set. A detailed description of the model equations and numerical algorithms can be found in the paper by *Stammer et al.* [1996] and references therein. Our analysis will be focused on the experiment POCM-4C that was run for the 19-year period 1979–1998. From 1979 to 1994, the model was forced with daily atmospheric fluxes derived from the European Center for Medium Weather Forecast (ECMWF) reanalysis; after that time period, the forcing fluxes were replaced with operational ECMWF data sets. For the purposes of this article, we use 3-day averages (separated by 9 days) of model outputs of temperature, salinity, velocity and sea surface height (SSH) corresponding to the period 1986–1998.

3. Results

3.1. General Circulation

[5] The mean circulation patterns of POCM are characterized by the general eastward flow of the ACC in the subpolar region, and anticyclone gyres in each of the subtropical basins (Figure 1). The ACC is composed of three broad jets, whose locations roughly correspond with the Subantarctic Front (SAF), the Polar Front (PF) and the Southern ACC Front (SACCF) [*Nowlin and Klinck*, 1986]. The path of the northernmost of these jets undergoes wide meridional excursions, but the southern ones are very stable. After passing through the Shackleton Fracture Zone, located at ∼66°W, the two northernmost jets merge and divert most of the ACC transport (∼106 Sv) to the northern portion of the Drake Passage. Such a concentration of the ACC transport is in agreement with the observations of *Cunningham et al.* [2003], who reported that the northern portion of the Drake Passage composes nearly 90% of the total ACC transport. After rounding the Burdwood Bank, the ACC splits into two branches: the west branch (WB), which carries approximately half of the MC transport (∼35 Sv) and flows northward along the continental slope of South America, and the east branch (EB), which contributes with the remaining half of the MC transport and flows eastward along the Polar Front. The confluence of the two branches, which occurs near ∼48°S, forms the MC, which continues its northward progression until its collision with the southward flow of the BC at ∼45°S. The mean transport of the MC varies from 69.7 Sv at 50°S to 54.4 Sv at 40°S. *Vivier et al.* [2001] computed a value of 41.4 Sv at 41°S. A direct comparison between model and observations is not possible because the southward displacement of the Brazil/Malvinas Confluence in the model.

[6] The two most obvious shortcomings of the circulation patterns simulated by POCM are the magnitude of the volume transport of the ACC and the location of the Confluence. The ACC transport in POCM is 163 ± 6 Sv, which is higher than the 134 ± 13 Sv estimated from observations [*Nowlin and Klinck*, 1986]. This deficiency has been attributed to the lack of spatial resolution. *Gille* [1997] showed that although POCM has relatively high eddy kinetic energy levels over major topographic formations (e.g., the Kerguelen Plateau in the Indian Ocean, the Campbell Plateau south of New Zealand and the Drake Passage) the model does not reproduce the kinetic energy levels of other regions in the Southern Ocean and, therefore, does not generate enough topographic stress to balance the input from the wind forcing. The lack of skill of POCM to simulate the correct location of the Confluence is a common trait of most eddy-permitting global ocean models. As shown in previous studies, the location of the Confluence is very sensitive to small changes of transport of two large currents and the representation of the bottom topography [*Matano*, 1993; *Agra and Nof*, 1993]. In the numerical simulations of *de Miranda et al.* [1999], for example, the transport of the MC is ∼80 Sv and the Confluence is located near ∼30°S. Conversely, in the more recent CLIPPER simulations the Confluence is located at ∼45°S [*Treguier et al.*, 2001].

[7] In spite of the deficiencies noted above, POCM seems to reproduce reasonably well the broad characteristics of what is known about the low-frequency variability of the ACC and MC transports. To assess the model's skill, we first compared transport time series calculated from the model with subsurface pressure (sea level corrected for the inverse barometer effect) time series collected at Faraday Station (Figure 2) (see Figure 1 for station location). This comparison was guided by the study of *Meredith et al.* [2004], who showed that subsurface pressure at this location is a useful proxy to monitor the interannual variability of the ACC transport. The correlation between POCM and observations is $r \sim -0.7$ (the critical value at the 99% significance level is -0.66). POCM also appears to represent reasonably well the seasonal evolution of the transport of the MC. To test the model's skill, we compared the monthly mean evolution of the MC transport from POCM (section MC in Figure 1) with the values derived from in situ observations (at ∼41°S) by *Vivier and Provost* [1999] (Figure 3). In this study, the MC section is located at ∼50°S to minimize the influence of the returning flow of the MC as well as the mesoscale eddies originated in the Confluence, which is abnormally located at ∼45°S. The transports were computed from the area integral of the cross-sectional velocities regardless of their signal. There is good agreement between the phases of the seasonal evolution of the model and observations, although the latter shows a stronger semiannual component than the model. Both data sets show a weakening of the MC transport toward the fall, with an absolute minimum between March and April, and a strengthening toward the middle of the winter, with an absolute maximum between June and July. The main discrepancy between POCM and observations is the amplitudes of the anomalies (∼5 Sv in observations and ∼3 Sv in the POCM).

3.2. Links Between the ACC and the MC

[8] Within the limitations of the existing data records, POCM appears to capture reasonably well the low-frequency variability of the ACC and the MC. Therefore, in what follows, we use the model results to investigate the dynamical links between them. First, we compare the transport time series of both currents (Figure 4). The correlation between them is relatively low ($r \sim 0.45$, the critical value at the 99% significance level is ∼0.22), considering the short distance that separates them, but increases substantially

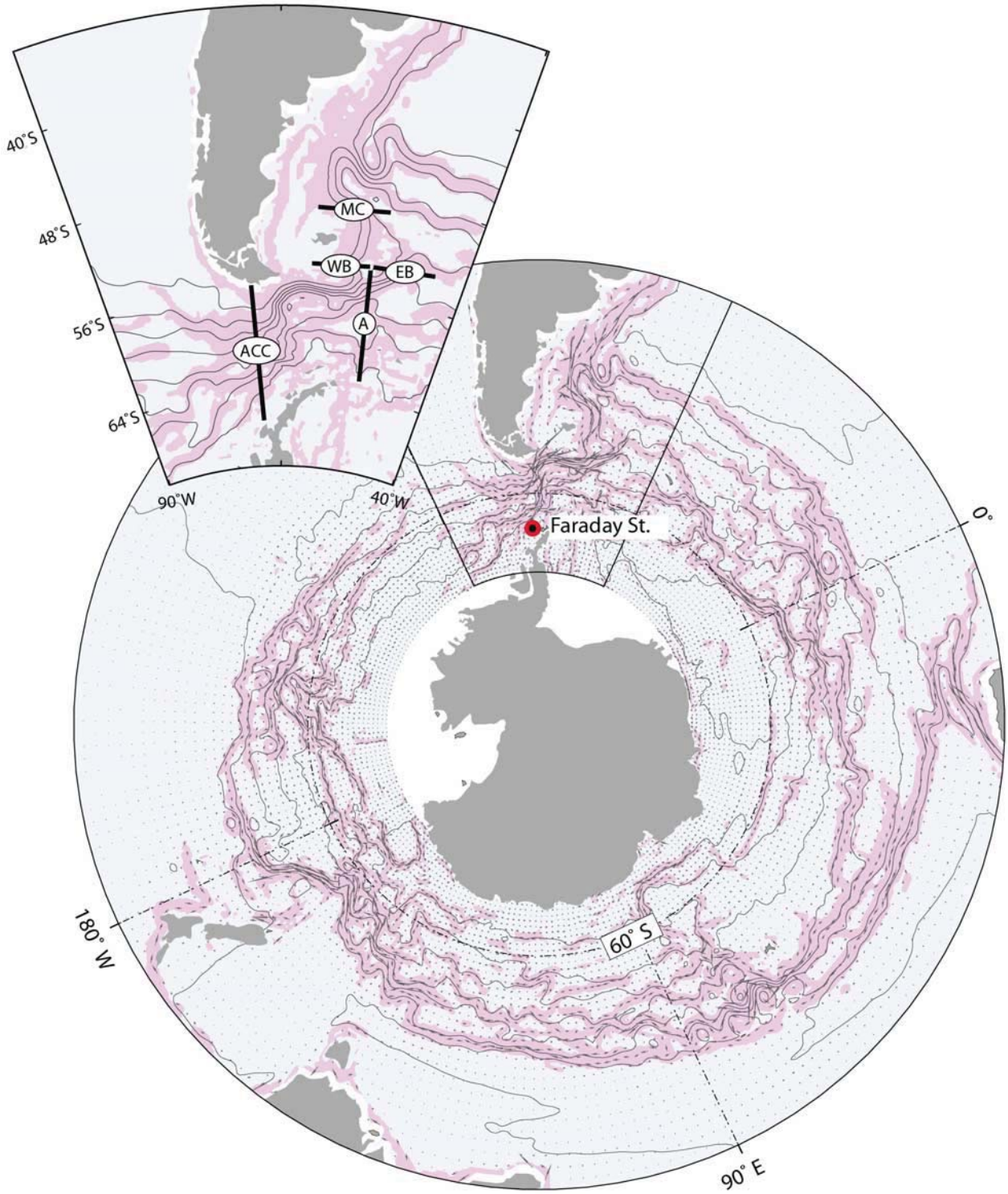

Figure 1. The model domain showing the mean stream function (contours) and the vertically averaged velocity field. Red shaded areas indicate the regions where the depth-averaged velocity is larger than 10 cm s^{-1}. The inset shows the location of the ACC section at the Drake Passage, the east and west branches, the Malvinas Current, and section A. The location of Faraday (Vernadsky) Station is also shown.

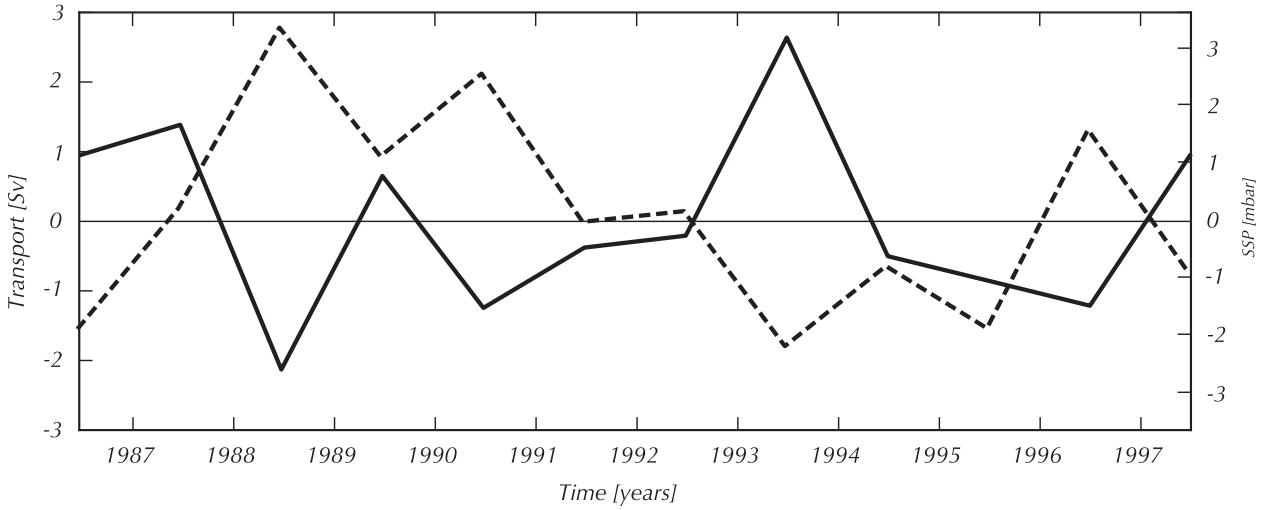

Figure 2. Annual anomalies of the ACC at the Drake Passage (solid line) and subsurface pressure (sea level corrected for the inverse barometer effect (dashed line)) measured at the Faraday Station (see Figure 1 for station location).

($r \sim 0.7$, the critical value at the 99% significance level is $\sim$0.53) if the time series are low-pass filtered to remove oscillations with periods shorter than 6 months, which indicates that the connection between the ACC and the MC transports is masked by high-frequency variability. There is only scant observational data to confirm this result. *Vivier et al.* [2001] showed that the most significant coherences between bottom pressure variations in the southern part of the Drake Passage and transport variations of the MC occur at periods longer than 4 months, however, they found a small lag of $\sim\pi/4$, where a lag of π would be expected if the MC was driven by oscillations of the ACC at the Drake Passage. (Note that an intensification of the ACC should be related to a drop of bottom pressure at the southern part of the Drake Passage.)

[9] In what follows, we will try to determine the dynamical processes that degrade the coherence between the transport variations of the ACC and the MC. As a first step in that direction, we computed the power spectra of cross sections extending from the Drake Passage to the MC (Figure 5). Individual spectral estimates are chi-square distributed with two degrees of freedom. One way to reduce the variance of such a noisy estimate is to split the long time series into shorter ones, and then, average the spectra of the short time series. To increase the number of degrees of freedom of the final estimate and improve its statistical significance, one can extract the short time series with some degree of overlapping between them. In this computation, we chose to use 50% of overlapping, which produces $\sim$1.9 degrees of freedom per estimate (0% overlapping would produce 2 degrees of freedom). Finally, to reduce the edge effects produced by the finite length time series, all short time series were extracted from the long one by applying a Hanning window. Also, the spectra were normalized to preserve the total variance of the time series. The most energetic signals at the Drake Passage are the annual and semiannual cycles, although there are also statistically significant peaks at subseasonal timescales (3–4 months). The EB shows a significantly higher level of high-frequency variability (periods shorter than 1 year) than the WB and the MC. The MC has the same level of annual variability as the WB, but a higher level of semiannual variability. A superposition of the different power spectra shows that the MC has a lower level of high-frequency variability than the EB. There are no significant semiannual peaks in the WB, but there are in the EB and the MC. All four spectra have a

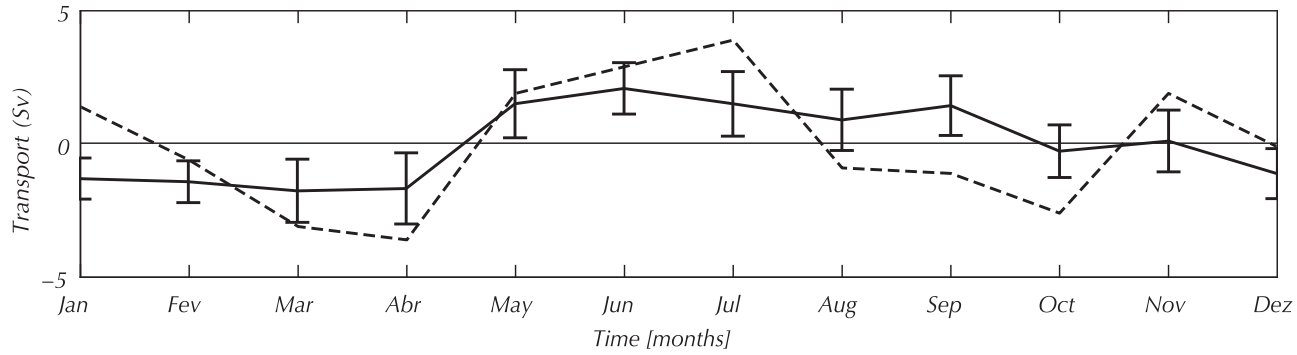

Figure 3. Monthly transport anomalies of the Malvinas Current from POCM (solid line with 99% significance level confidence interval) and from *Vivier and Provost* [1999] (dashed line).

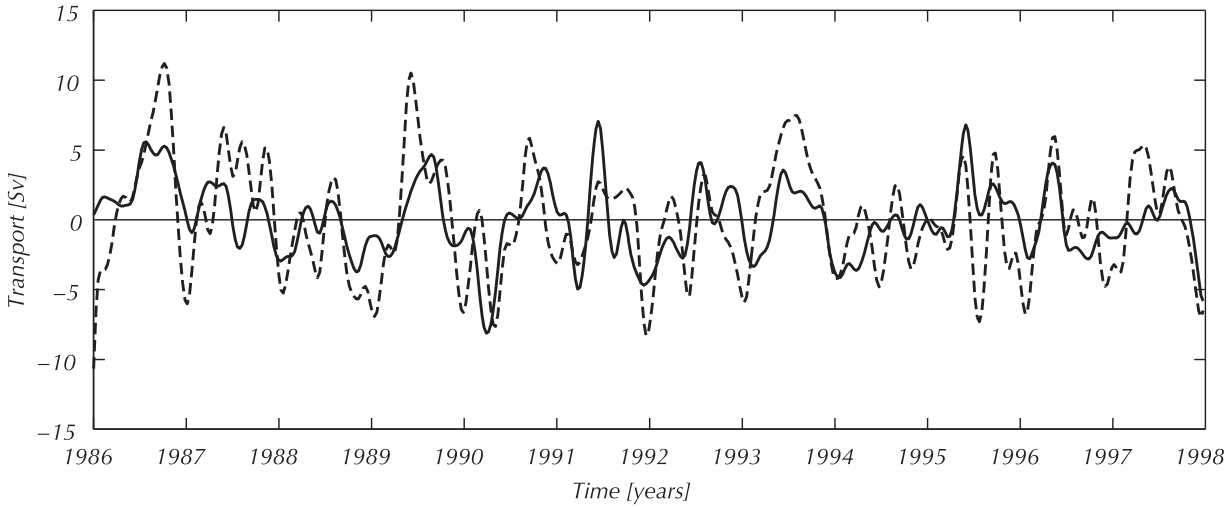

Figure 4. Transport anomaly time series of the ACC (dashed line) and of the Malvinas Current (solid line) in POCM (see Figure 1 for section locations).

significant peak at ∼150 days, which, as we shall show, is associated with the propagation of perturbations originating at the Drake Passage. Thus, the spectral analysis suggests that most of the high-frequency variability present at the Drake Passage is funneled to the EB. It also suggests that the semiannual peak in the MC, which has also been reported from observations [*Provost et al.*, 1992; *Goni et al.*, 1996; *Vivier and Provost*, 1999], is either generated locally or advected from the Drake Passage through the EB.

[10] To corroborate the preliminary conclusions derived from the spectral analysis, we calculated the mean transport, variance and spectral density estimates of the cross sections just described (Figure 6). The spectra were computed in a similar way of the spectra of Figure 5. The cross section at the Drake Passage shows two jets with a velocity maximum near 62°S. The largest velocity variances and most of the high-frequency variability are concentrated in the southern portion of the passage, while the northern flow shows lower levels of high-frequency variability. The spectral distribution of the EB and WB resemble those of the northern and southern portions of the Drake Passage, respectively. The spectrum of the EB is fairly white and the spectrum of the WB is dominantly red. Note that the region with the largest transport (∼53.5°W–54.5°W) has insignificant levels of energy at periods shorter than 3 months. The spectral distribution in the MC cross section closely resembles that of the WB. The center of the jet, which is located between 53°W and 54°W, has its most significant peaks at the annual and semiannual periods. The largest variances in the eastern side are driven largely by instabilities generated at the Confluence. Thus, the spectral analysis suggests that the high frequency of the ACC is largely funneled to the EB, and from there, to the PF and not to the MC.

[11] To confirm the results of the spectral analysis, it still has to be shown that the high-frequency oscillations present on the southern part of the ACC at the Drake Passage reach the bifurcation point. To prove that, we computed the coherence and phase spectra between the transport time series of the ACC, the MC, the WB and section A in Figure 1. Section A was chosen, instead of the EB, to conserve mass in the analysis, for there is a small fraction of the circumpolar flow that does not cross the WB and EB. Hence, the flow through section A represents the part of the circumpolar transport that does not bifurcate to form the WB. The coherence spectrum between the ACC and the WB transports is similar to the spectrum between the ACC and the MC transports (Figures 7a and 7b). In that, the main peaks are centered at the annual cycle. The main difference is an oscillation of ∼3 months in the spectrum between the ACC and the WB transports, while the coherence between the ACC and the MC shows a marginally significant peak for an oscillation of ∼4 months. The coherence between the ACC and section A is statistically significant for almost the entire frequency range (Figure 7c). The nearly perfect coherence between the ACC and the combined transports of the WB and section A confirms that the variability of the ACC in the Drake Passage indeed reaches the bifurcation point (Figure 7d). The zero phase expresses the fast barotropic adjustment of the ACC oscillations [*Wearn and Baker*, 1980; *Peterson*, 1988; *Hughes et al.*, 1999; *Gille et al.*, 2001; *Weijer and Gille*, 2005]. Thus the coherence analysis shows that the high-frequency oscillations found on the southern part of the ACC reach the bifurcation point, but instead of following the coast of South America toward the MC section, these anomalies are funneled to the part of the ACC flow that does not bifurcate to form the MC flow downstream. These high-frequency oscillations degrade the correlation between the ACC and the MC transports.

[12] The links between the seasonal variations of the ACC and the MC have been a subject of particular interest in previous studies [e.g., *Olson et al.*, 1988; *Matano et al.*, 1993; *Smith et al.*, 1994; *Gan et al.*, 1998; *Wainer et al.*, 2000]. To investigate these matters using POCM results, we computed the monthly mean transport anomalies of the cross sections of the ACC, EB, WB and MC (Figure 8). The ACC has positive transport anomalies during all seasons except summer. The EB, WB and MC have positive anomalies during the winter and negative anomalies during the summer, which indicates that the seasonal variations of the ACC transport are equally transmitted to both branches.

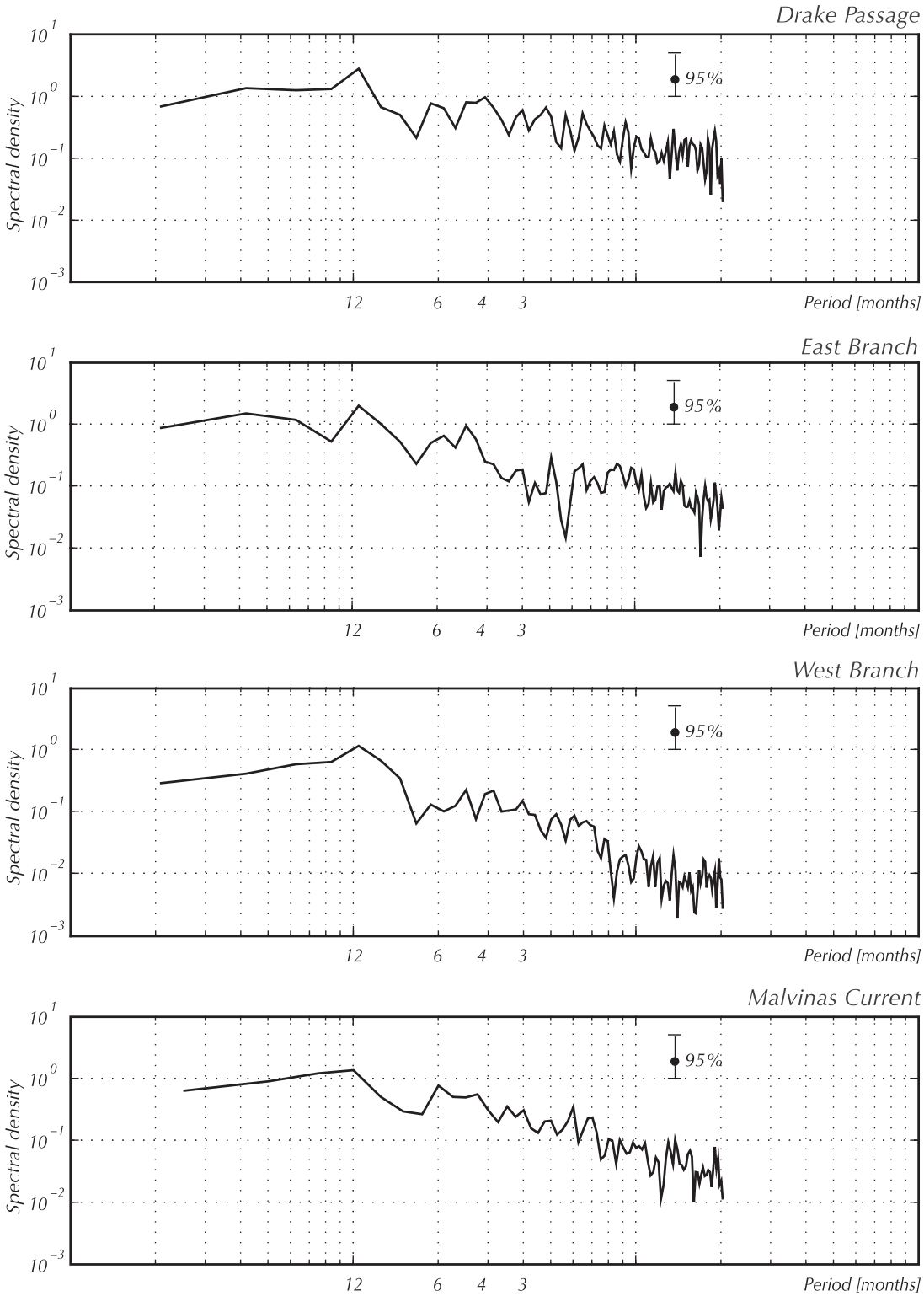

Figure 5. Spectral density estimates of the transport time series of the ACC, the west branch, the east branch, and the Malvinas Current (see Figure 1 for section locations).

One interesting characteristic of the model results is the relative smallness of the seasonal variations. The amplitude of the seasonal cycle at the Drake Passage is ~3 Sv and of the MC is ~2 Sv. The seasonal variations of the ACC transport are less than 2% of its total transport. Those in the MC are relatively larger but they still account for less than 4% of its volume transport. The relative smallness of the seasonal variations in the ACC and the MC might explain why it has been difficult, in observations, to find correlation between these two currents. The smallness of the signal,

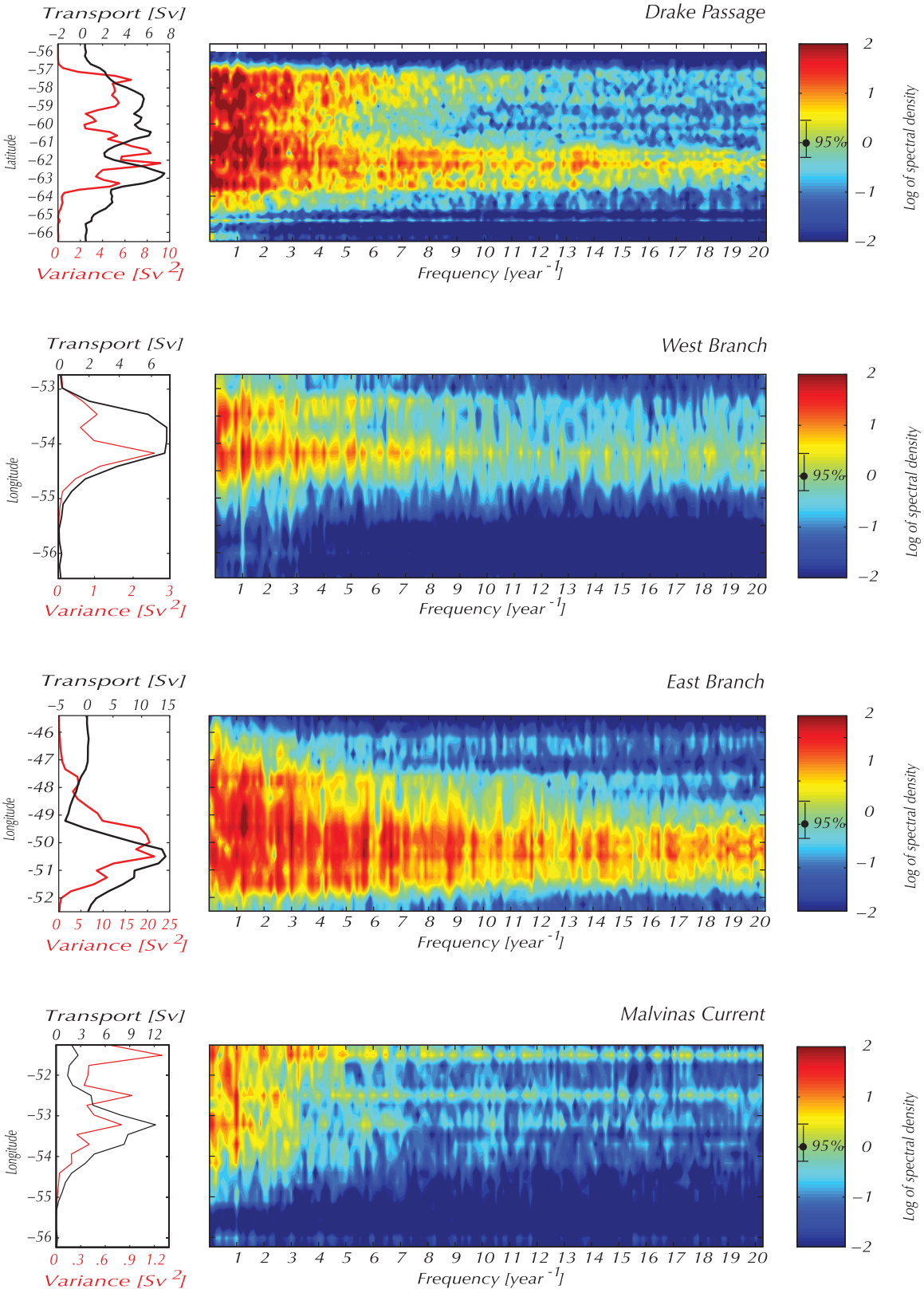

Figure 6. (left) The mean transport (black line) and the variance (red line) of the ACC, the west branch, the east branch, and the Malvinas Current (see Figure 1 for section locations). (right) Spatial distribution of the spectral density estimate of the vertically integrated transport across the same sections.

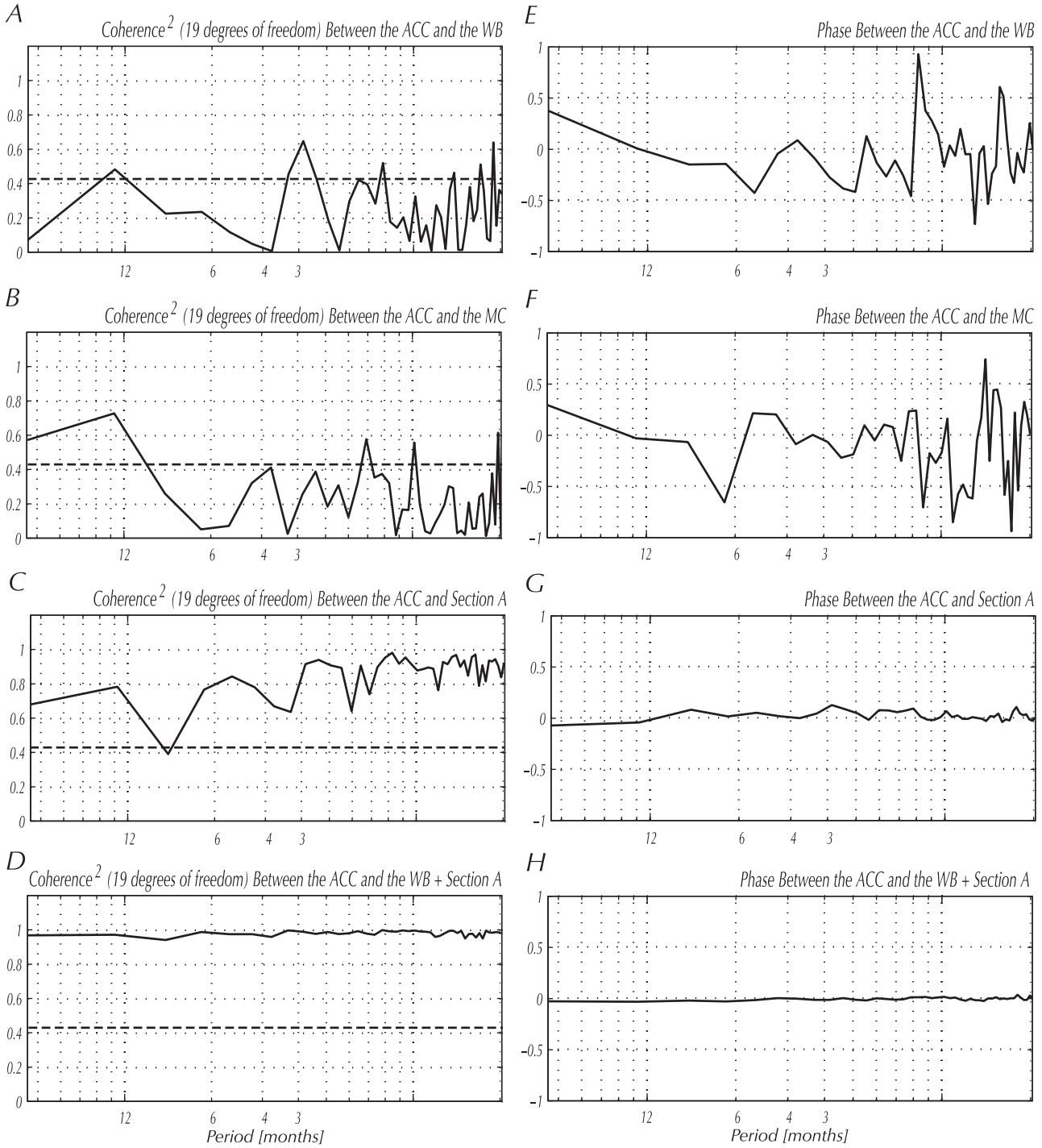

Figure 7. Squared coherence between the transport time series of (see Figure 1 for section locations) for (a) the ACC and the west branch, (b) the ACC and the Malvinas Current, (c) the ACC and section A, and (d) the ACC and section A plus the west branch. Also shown, the phase spectra of (divided by π) the ACC and the west branch (Figure 7d), (e) the ACC and the Malvinas Current, (f) the ACC and section A, and (g) the ACC and section A plus the west branch.

however, is further masked by the high-frequency variability of the ACC.

3.3. Propagating Anomalies

[13] Although a substantial portion of the high-frequency variability that masks the correlation between the ACC and the MC is produced and dissipated locally, there are also anomalies that propagate between these regions. While these anomalies are important because they create dynamical linkages, they can also degrade the coherence between the two currents. During the last few decades, several authors have documented the generation and propagation

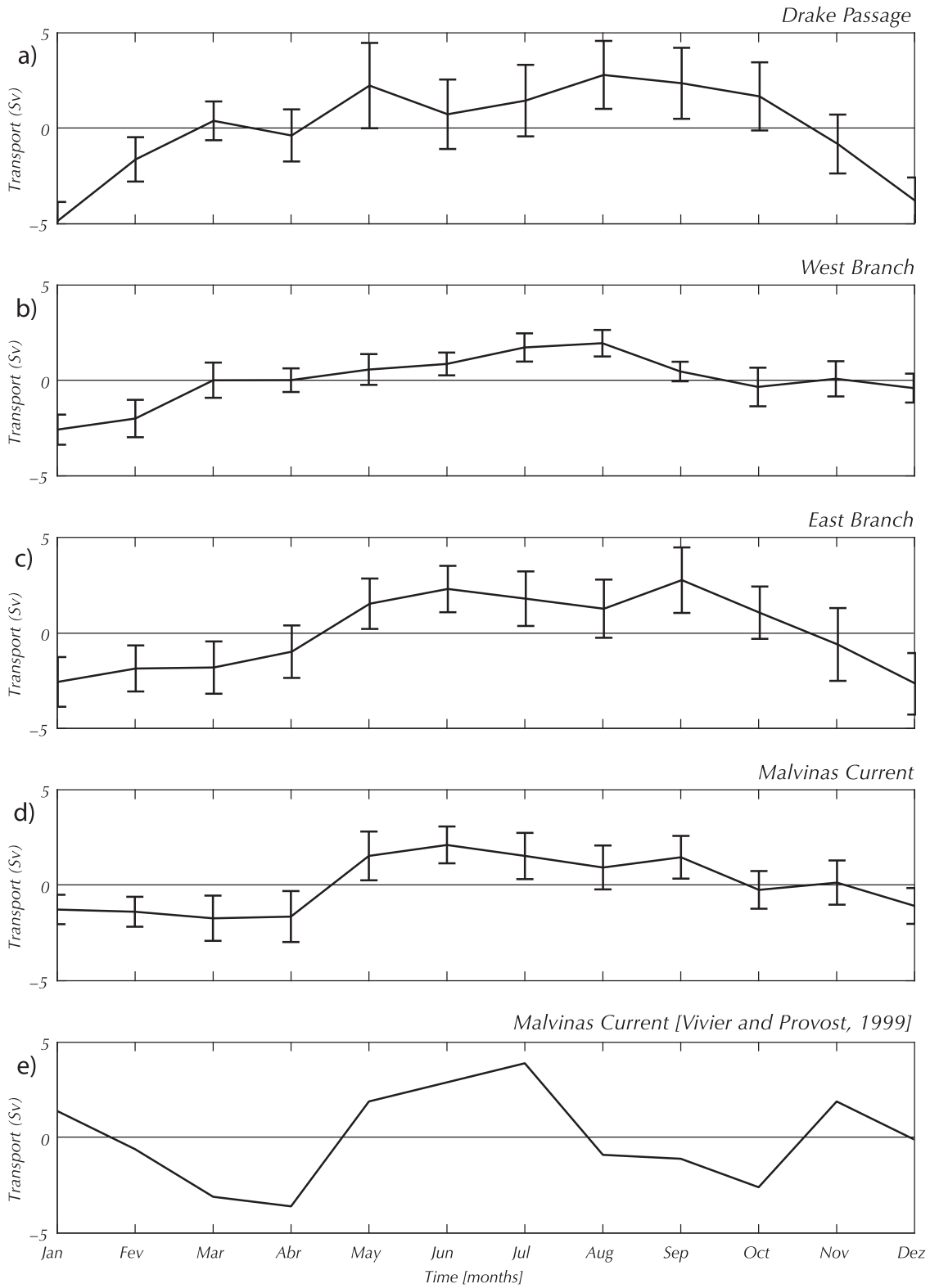

Figure 8. Monthly transport anomaly time series with 99% significance level confidence intervals of (a) the ACC, (b) the west branch, (c) the east branch, and (d) the Malvinas Current (see Figure 1 for section locations). (e) Transport anomalies of the Malvinas Current as computed by *Vivier and Provost* [1999] from current meter measurements.

of mesoscale perturbations in this region. *Inoue* [1982] reported eddies propagating with phase speeds of 9–20 cm s^{-1}. *Hofmann and Whitworth* [1985] observed the formation of four large rings (100 km in diameter) in the PF that propagated to the northeast with phase speeds of 5–10 cm s^{-1}. *Sprintall* [2003] found eddies, with mean diameters of 50–100 km, that were advected to the north-northeast by the ACC. *Fu* [2006] observed eddies propagating from the Drake Passage toward the EB and the WB with speeds of ~7 cm s^{-1} and from there toward the Confluence and the Zapiola Anticyclone regions. *Fu* [2007] also found that 25-day oscillations in the Zapiola Anticyclone are coherent with the mesoscale variability in the period range of 100–150 days. In the most comprehensive study of the variability of the MC, *Vivier et al.* [2001] analyzed 18 months of current meter measurements spanning a section of the MC near the Confluence. They concluded that the dominant mode of variability of the MC at that location was associated with annual migrations of the Subantarctic Front. They also showed the presence of an energetic oscillation with a period of ~140 days that was aligned with the bottom topography and was linked to the variability of the wind stress curl in the Drake Passage.

[14] POCM reproduces some of the characteristics reported in the observational record. The most conspicuous of the propagating signals in the model has an average period of ~150 days. It is generated at the entrance of the Drake Passage and is transmitted equatorward through the planetary potential vorticity (*f/H*) contours. To illustrate the propagation of this signal, we calculated a time-lagged correlation between time series of transport anomalies along the *f/H* lines connecting the Drake Passage with the WB and the EB (Figure 9). All time series were band-pass filtered to remove oscillations with periods shorter than 30 days and longer than 1 year. The maximum correlation corresponds to the reference point with itself and it decreases upstream and downstream (Figure 9). The linear trend in the phase plots, which extends from the Drake Passage up to the end of the paths, indicates a propagating signal. The speed of propagation of these anomalies, which is given by the slope of the lines, is ~6–7 cm s^{-1} in both cases (through the EB and WB paths). To further corroborate the existence of these propagating anomalies, we also computed the coherence and phase between the reference point and a point located just before the branching of the two paths (not shown). According to the time shift theorem of the Fourier transform [e.g., *Bracewell*, 2003], the linear trend of the phases indicates a constant time lag between these points. The speed of propagation of the anomalies can be calculated as the ratio between the distance of the reference points and the time lag from the phase diagram. We obtained the same speed of propagation found when using the time-lagged correlation approach (~6–7 cm s^{-1}). This methodology is sensitive to the choice of the analyzed points. In order to verify the robustness of these results, we decided to repeat the same computation using a point after the reference point (not shown). The result is similar to the result of the previous analysis, which shows a downstream propagation of the signal at a speed of ~6–7 cm s^{-1}.

[15] For a more comprehensive characterization of propagating anomalies, we calculated the Complex Empirical Orthogonal Function (CEOF) [e.g., *von Storch and Zwiers*, 1999; *Emery and Thomson*, 2001] of the model's sea surface elevation. The first CEOF, which explains approximately 80% of the total variance, shows an amplitude maximum along the northern branch of the ACC (Figure 10a). Its phase shows a strong gradient, which is characteristic of propagating signals, within the Drake Passage and through the WB and the EB (Figure 10b). However, the CEOF amplitudes in the EB and the WB are substantially smaller than those within the Drake Passage. The time series of the phase is dominated by ~150-day oscillations (Figure 10d). Most of the 150-day perturbations are generated to the west of the Shackleton Fracture Zone. We do not know the origin of these perturbations. We surmise that they may be triggered by instabilities of the ACC associated with its entrance to the Drake Passage. Upon reaching the point where the ACC bifurcates into the WB and the EB, these oscillations generate out-of-phase variations of both branches that decrease the correlation between the ACC and the MC (Figure 11). The passage of the trough of the wave increases the transport of the WB and decreases the transport of the EB. Half a period apart, the process is reversed by the passage of a crest, which increases the EB transport and decreases the WB transport. Although ~150 days is the dominant period, this phenomenon is observed in a broader range of temporal scales, including the interannual (Figure 12).

[16] To investigate whether the 150-day oscillations observed in the model are also found in the real ocean, we applied the CEOF technique to ~14 years of weekly mean sea surface height anomalies (SSHA) from Archiving, Validation, and Interpretation of Satellite Oceanographic data [*Ducet et al.*, 2000], and ~4.5 years of weekly mean sea surface temperature anomalies (SSTA) from the Advanced Microwave Scanning Radiometer (AMSR) [*Chelton and Wentz*, 2005; F. J. Wentz and T. Meissner, unpublished data, 2000]. As in our previous calculation, we band-pass filtered all time series to remove oscillations with periods smaller than a month and longer than 1 year. The first CEOF explains ~18% of the SSHA variance and shows anomalies that propagate through the Drake Passage at velocities of ~3–6 cm s^{-1}, with an average period of ~165 days (Figures 13a, 13b, 13c, and 13d). There is a clearer signal of northward propagation through the EB than through the WB. The time series of the CEOF indicates that, while during some years (e.g., 1998) there was almost one oscillation per year, during others (e.g., 2003) the number of oscillations tripled. CEOF analysis is most useful to identify propagating signals with a relatively narrow frequency band. Broadbanded signals do not allow the CEOF decomposition to separate the propagating oscillations in orthogonal modes, for these signals may not be orthogonal to each other. The first CEOF of the SSTA shows no propagation through the Drake Passage. The second CEOF, which explains ~16% of the SSTA variance, shows a weak propagating signal at the Drake Passage and near to the bifurcation point (Figures 13e, 13f, 13g, and 13h). As for the CEOF decomposition of the SSHA data, the propagation of SST anomalies is stronger through the EB than through the WB. The fast degradation of the SST signal, which makes it difficult to capture its propagation, is probably due to the intense air-sea interactions that take place at these latitudes. The SST oscillations have an average period of

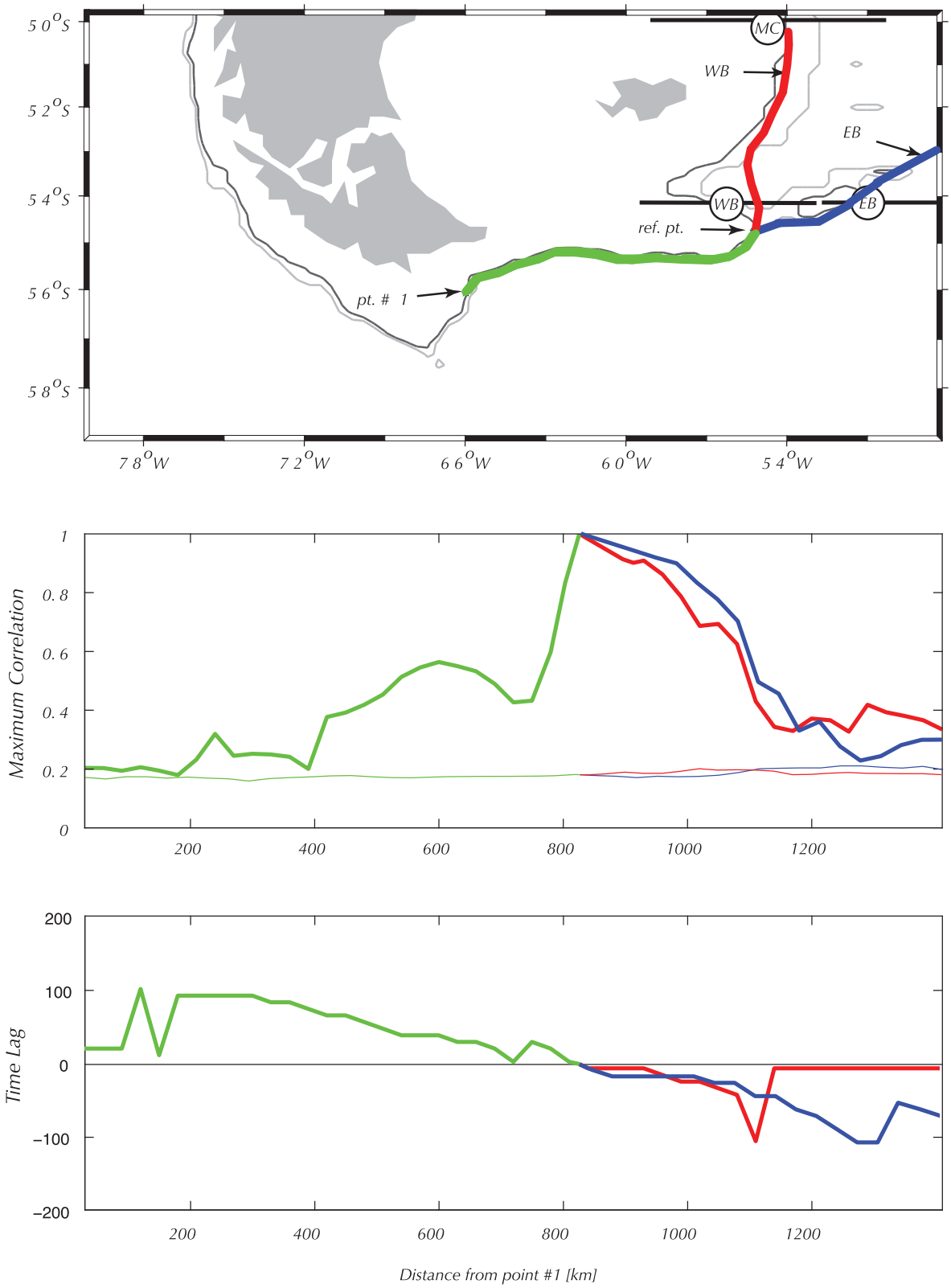

Figure 9. (a) The paths along the Drake Passage and following the west and east branches mean flow; (b) the maximum time-lagged correlation between the along-path transport time series of the reference point and the along-path transport time series of all the points along the paths in Figure 9a (thick lines), also, the 99% significance level critical value for those correlations (thin lines); and (c) the time lag (in days) at which the maximum correlation between the transport time series of the reference point and each of the points along the paths in Figure 9a has occurred. Green is the path along the Drake Passage, red is the west branch, and blue is the east branch.

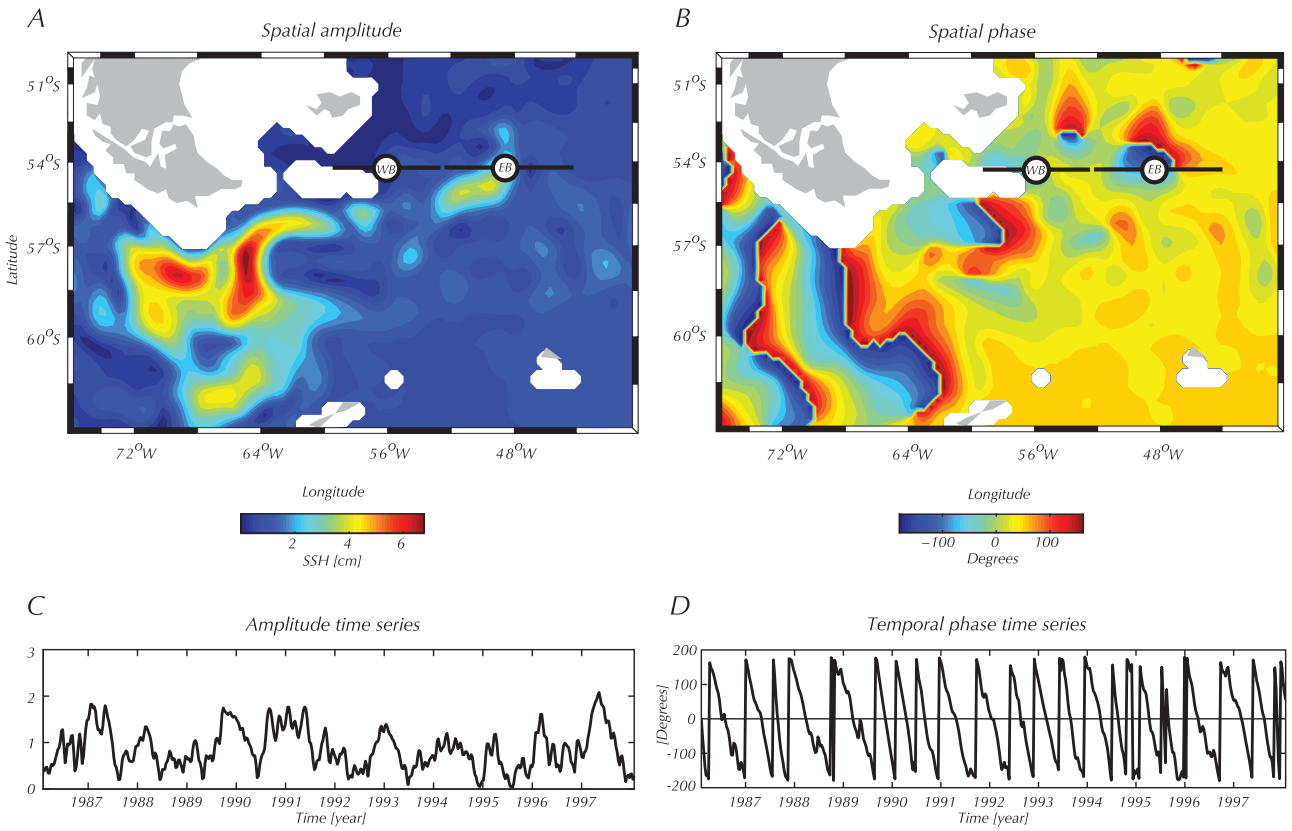

Figure 10. Complex empirical orthogonal function of the analytical signal of surface elevation from POCM showing (a) spatial amplitude, (b) spatial phase, (c) amplitude time series, and (d) temporal phase time series.

~165 days and propagation velocities similar to the SSH anomalies (~3–5 cm s^{-1}).

3.4. Influence of the Wind Forcing on the Variability of the ACC and the MC Transports

[17] To determine the covariability patterns between the ocean and the atmosphere, we computed the Principal Estimator Patterns (PEP) [e.g., *Davis*, 1977, 1978; *Strub et al.*, 1990] of the ACC and MC transports (sections ACC and MC) and the wind stress and the wind stress curl over the entire Southern Ocean. For the latter, we use the ECMWF wind data that was used to force POCM. All time series were low-pass filtered to remove oscillations with periods shorter than 30 days. PEPs identify coupled modes of variability between two spatial fields. These modes are formed from a linear combination of a rotated subset of the empirical orthogonal functions of the original forcing fields (e.g., the winds) and the forced fields (e.g., the cross-sectional velocities). A PEP decomposition yields the spatial amplitudes of the estimator and the estimand and the time series at which these fields oscillate together. This decomposition maximizes the variance of the estimand (Appendix A). The PEPs are computed from the time anomalies of the fields (the time mean at each spatial location is removed), therefore, the PEP fields can be interpreted as anomalies of the original fields superimposed to their means.

[18] The absence of meridional boundaries in the latitude of the Drake Passage (56°S–62°S) makes the dynamics of

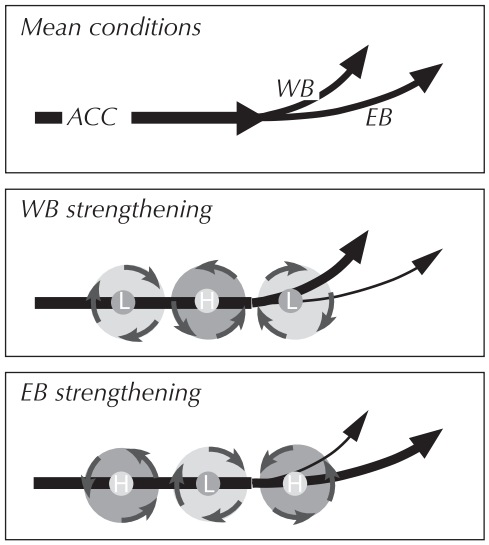

Figure 11. Schematic representation of the effect of propagating anomalies on the transport of the west and east branches. The velocity anomaly created by a sequence of low/high sea surface height anomalies at the bifurcation point reinforces the transport of the west branch and decreases the transport of the east branch; half of a period later, the sequence of high/low anomalies decreases the transport of the west branch and increases the transport of the east branch.

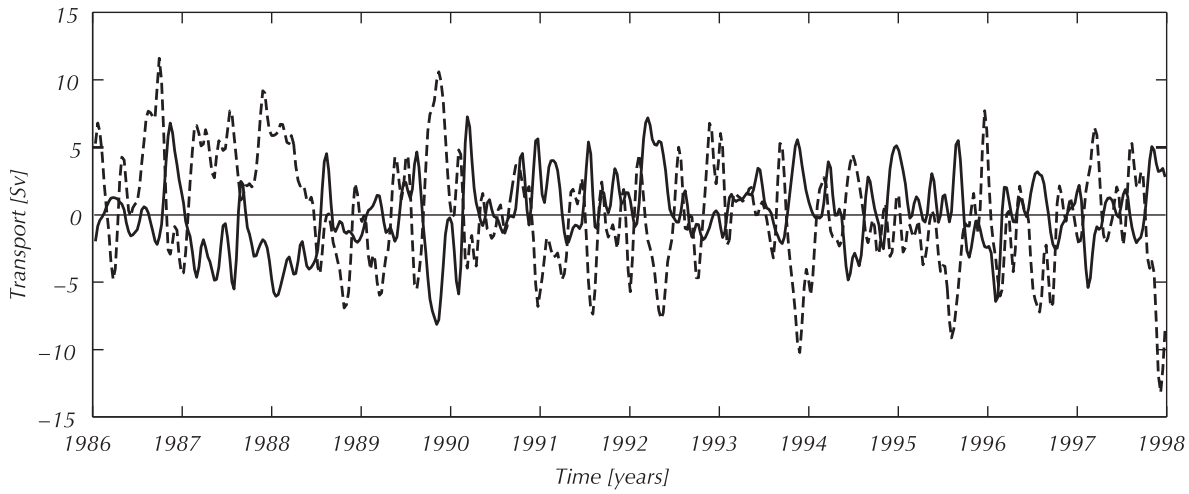

Figure 12. Transport anomaly time series of the west (solid line) and east (dashed line) branches in Figure 1.

the ACC unique among all ocean currents. Without meridional boundaries to support a pressure gradient, the net meridional geostrophic flow above unblocked depths has to vanish. There are two prevailing lines of thought. *Stommel* [1957] was the first to notice that only a few narrow bands of latitude are not blocked by land. *Stommel* [1957] suggested that the ACC transport is set by the Sverdrup transport at the southern most latitude of South America (~56°S). In his model, the MC would be the western boundary of this system, with the eastern boundary against the Antarctica Peninsula and the Scotia Island arc. *Munk and Palmén* [1951] pointed out that viscous dissipation could not match the wind stress. They proposed that the drag imposed by the pressure difference across major topographic features could balance the wind stress. How the surface wind stress is transmitted to the bottom and the final momentum balance is set by a complex interplay involving the surface forcings, eddy fluxes and friction [e.g., *Johnson and Bryden*, 1989; *Tansley and Marshall*, 2001]. Before we present this analysis, we should point out that our goal is not to unveil the true dynamical balance of the ACC and the MC. Rather, we seek to quantify how the transports of these currents are related with the broad, large-scale features of the wind field. Note also, that the wind stress and its curl are correlated. The PEP analysis is a purely statistical decomposition that is oblivious to the underlying dynamics, therefore, we anticipate that both the wind stress and its curl should be skillful on estimating the ACC and MC transports. That is supported by observational studies showing that the variability of the ACC and the MC is susceptible to variations of the wind stress and the wind stress curl over different portions of the Southern Ocean [e.g., *Peterson*, 1988; *Vivier et al.*, 2001; *Sprintall*, 2003].

[19] The first PEP of the ACC represents 33% of its variance and it is characterized by an approximation and acceleration of the Subantarctic and Polar fronts during the austral winter, and a separation and deceleration during the austral summer (Figure 14). These variations are congruous with an absolute maximum of the wind stress curl in the Pacific sector of the Southern Ocean (Figure 14). This result is in agreement with the findings of *Sprintall* [2003], who first noted that the variability of the ACC transport at the Drake Passage is correlated with similar variations of the wind stress curl and the wind stress in the southeast Pacific. The power spectrum of the time series of this mode shows statistically significant peaks at the annual, semiannual and ~150-day periods (not shown). The annual and semiannual peaks are clearly related to similar cycles in the atmosphere. The origin of the 150-day oscillation, however, is not clear; we surmise that it is an internal mode of variability generated by the interaction between the ACC and the bottom topography in the Drake Passage. As shown in the previous section, this mode is not an artifact of the model but is also present in the observations.

[20] The first PEP of the MC, which explains 32% of its transport variance, is congruous with a maximum of the wind stress curl at 50°S that extends from the Southeastern Indian Ocean to the Drake Passage (Figure 15a). These wind anomalies cause an acceleration of the offshore portion of the MC during late winter (September) and a subsequent reversal during summer (March) (Figures 15b and 15c). The fact that the first PEPs of the ACC and MC are related to variations of the wind forcing over nearly the same regions, and that the phases of their respective annual cycles are coincident (Figures 14 and 15), suggests that the offshore acceleration of the SAF in the Drake Passage causes an acceleration of the MC during the winter. This hypothesis was confirmed by an ancillary calculation (not shown) of the PEP of the ACC and MC, that PEP shows velocity profiles similar to those seen in Figures 14b and 15b.

[21] To complement the previous analysis, we also computed the PEPs of the wind stress and the ACC and MC velocities. The first PEP of the ACC shows a circumpolar belt of zonal wind stress anomalies in the latitudinal range of the Drake Passage that accelerates the ACC during the winter and decelerates it during the summer (Figure 16a). The large wind stress anomalies over the South Indian Ocean sector indicates that the atmospheric forcing in this basin is particularly important to the overall ACC variability, while the wind anomalies over the South Atlantic and

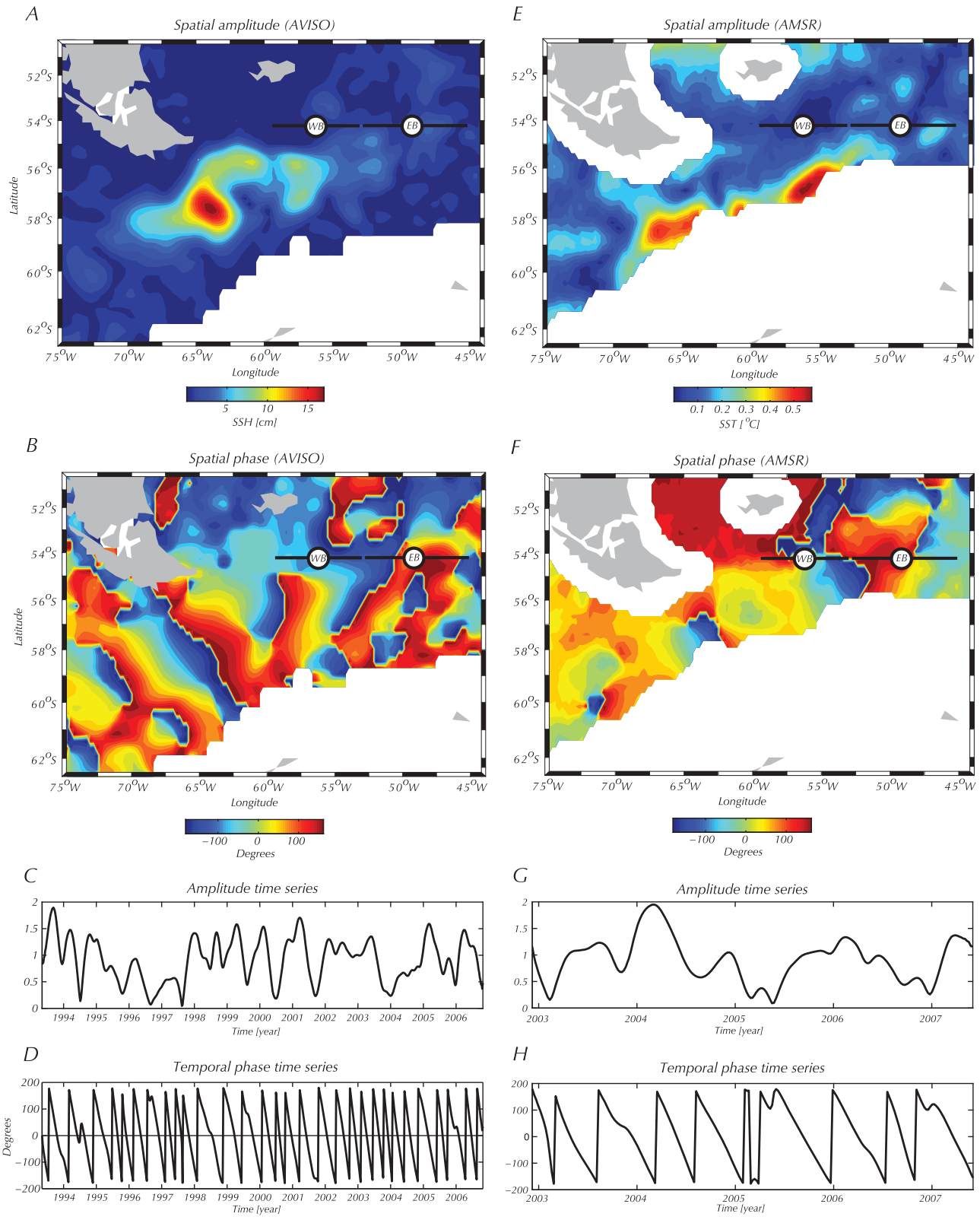

Figure 13. Complex empirical orthogonal function (a, b, c, d) of the surface elevation from Archiving, Validation, and Interpretation of Satellite Oceanographic data (April 1997 to October 2007) and (e, f, g, h) of surface temperature from AMSR (November 2002 to May 2007). Figures 13a and 13e show the spatial amplitudes, Figures 13b and 13f show the spatial phases, Figures 13c and 13g show the amplitude time series, and Figures 13d and 13h show the temporal phase time series.

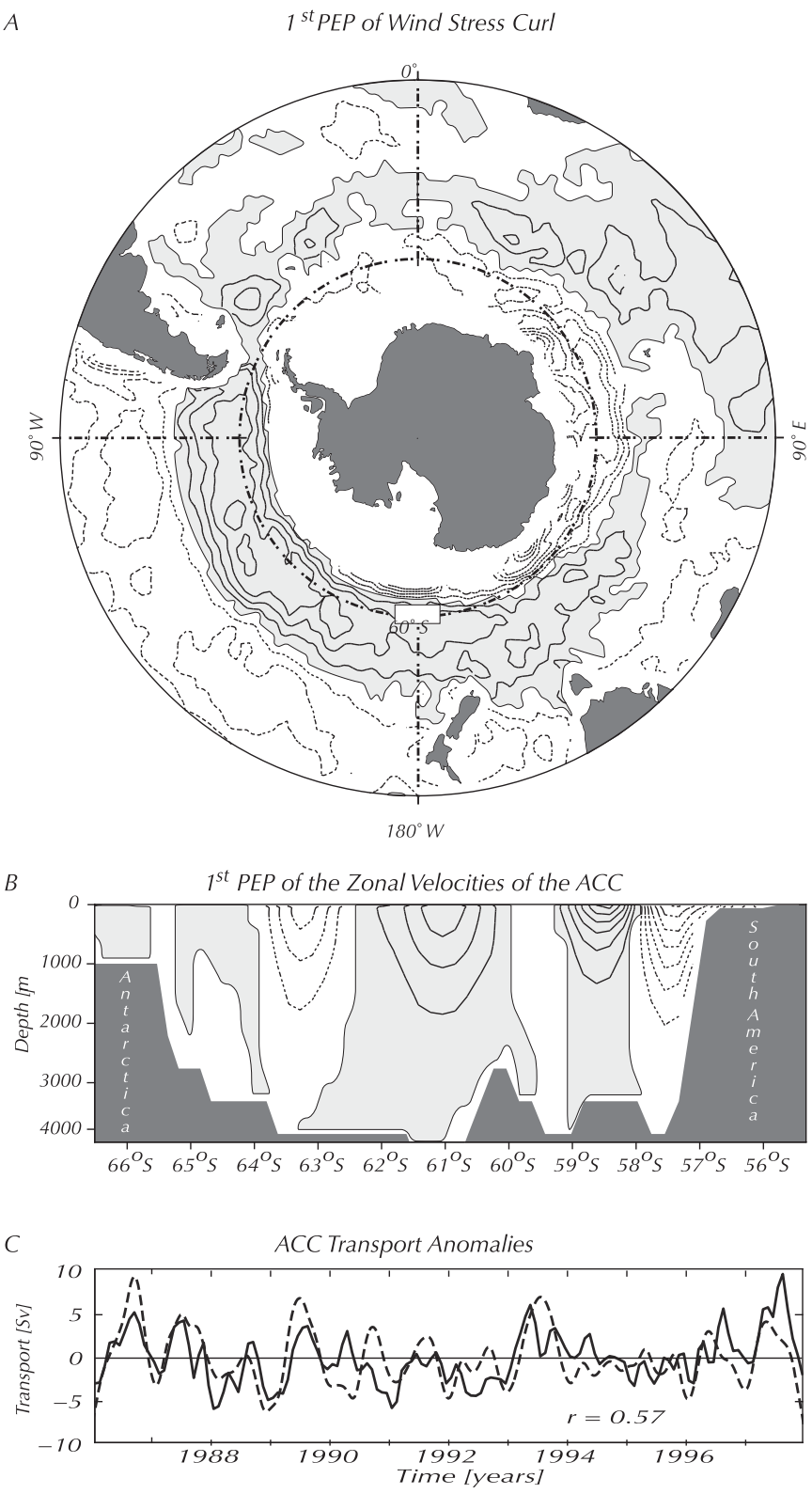

Figure 14. First PEP between the wind stress curl over the Southern Ocean and the zonal velocities of the ACC at the Drake Passage (Figure 1) showing (a) spatial amplitude of the wind stress curl (shaded area is positive, 2.10^{-8} N m^{-3} contour interval), (b) spatial amplitude of the zonal velocities of the ACC (shaded is positive, 2 cm s^{-1} contour interval), and (c) transport anomaly time series from the model (dashed line) and transport anomaly time series of the first PEP (solid line). The transport anomaly time series of the first PEP was generated by computing the area integral of Figure 14b and multiplying it by the amplitude time series of the first PEP (not shown). Therefore, those two time series differ by a normalization factor only. The PEP is presented such that the normalization factor is positive.

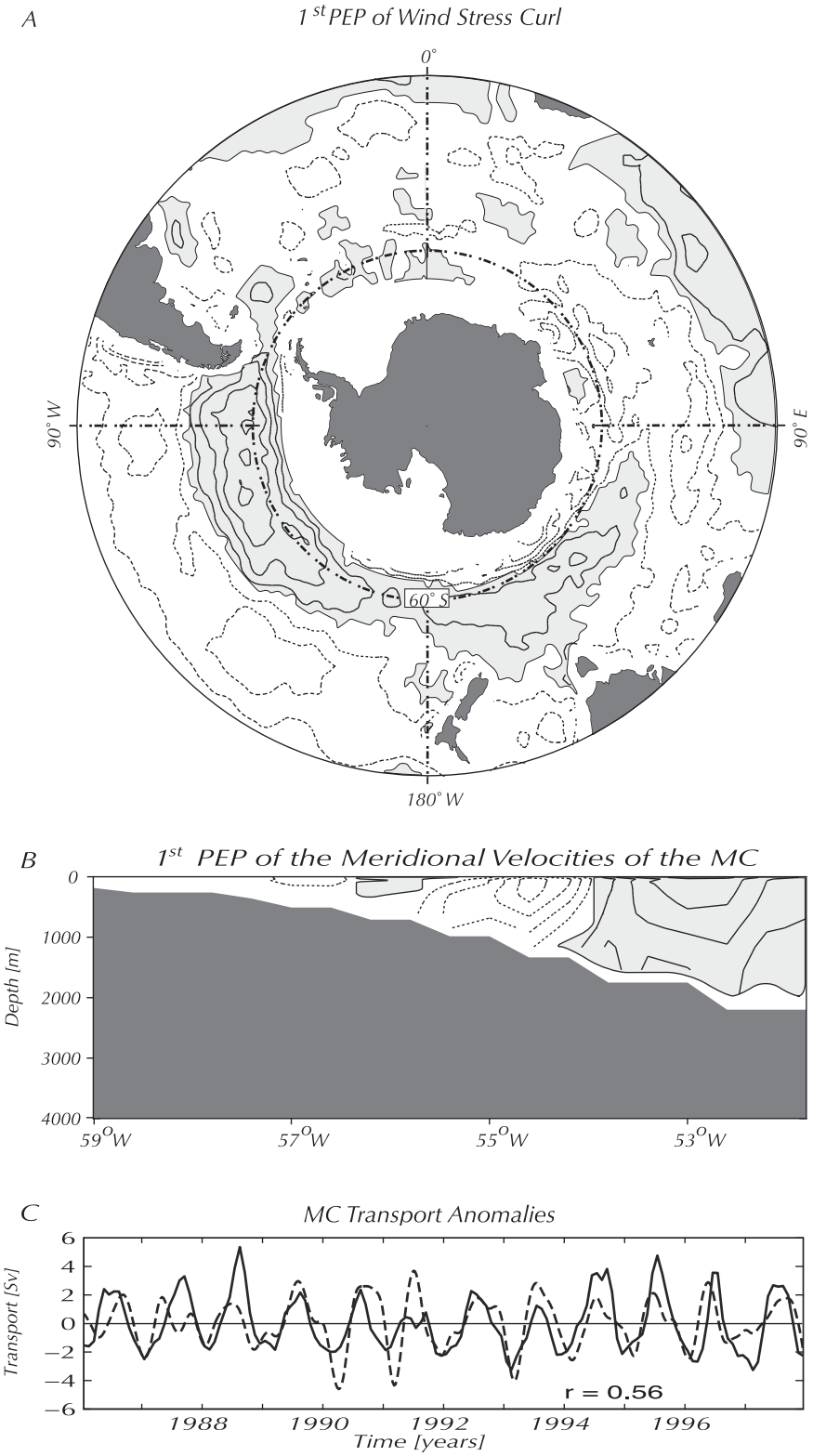

Figure 15. First PEP between the wind stress curl over the Southern Ocean the and meridional velocities of the Malvinas Current (Figure 1) showing (a) spatial amplitude of the wind stress curl (shaded area is positive, 2.10^{-8} N m^{-3} contour interval), (b) spatial amplitude of the meridional velocities of the Malvinas Current (shaded is positive, 0.5 cm s^{-1} contour interval), and (c) transport anomaly time series from the model (dashed line) and transport anomaly time series of the first PEP (solid line). The transport time series of the PEP was calculated as in Figure 14.

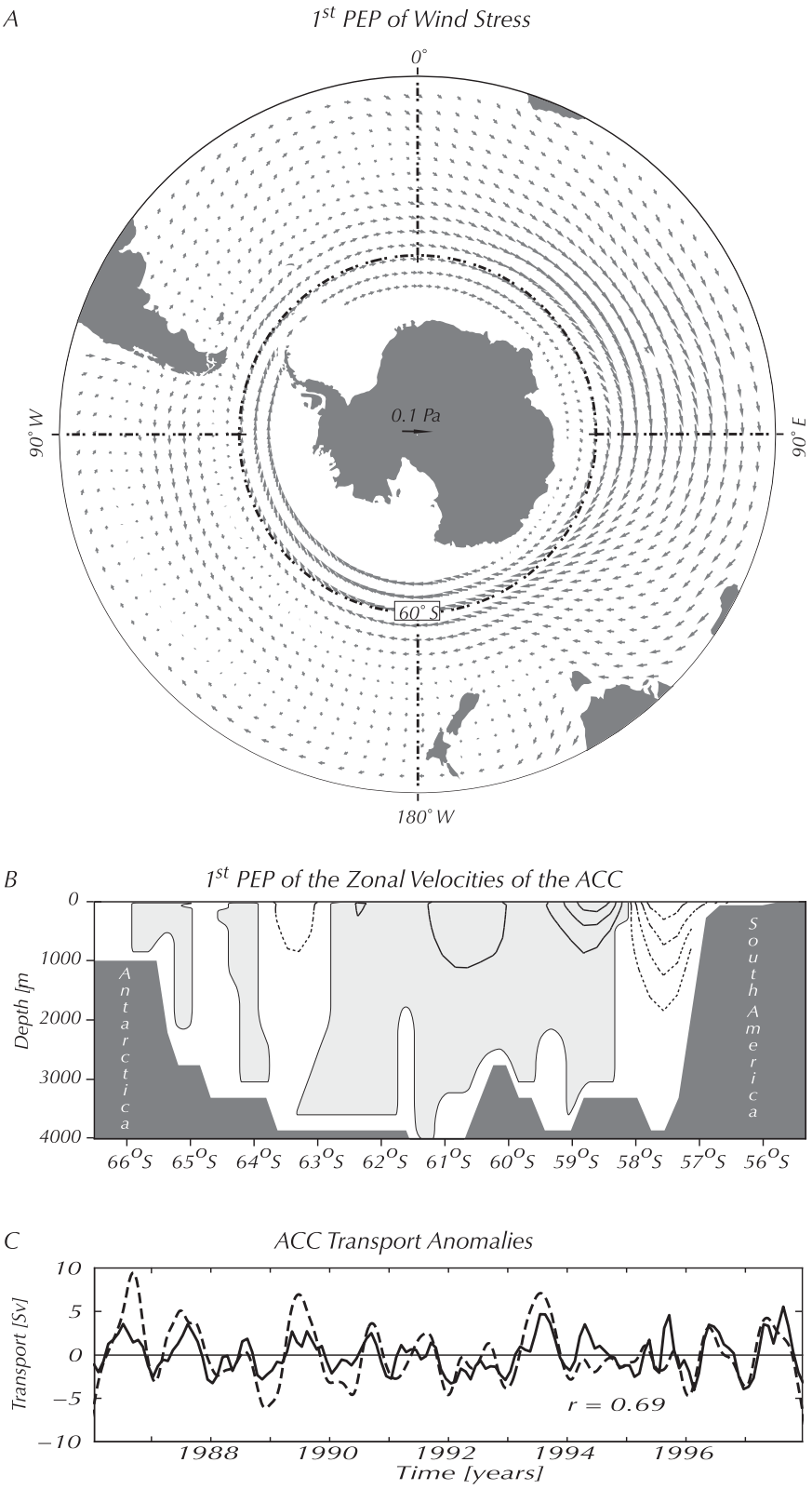

Figure 16. First PEP between the wind stress over the Southern Ocean and the zonal velocities of the ACC at the Drake Passage (Figure 1) showing (a) spatial amplitude of the wind stress, (b) spatial amplitude of the zonal velocities of the ACC (shaded is positive, 2 cm s^{-1} contour interval), and (c) transport anomaly time series from the model (dashed line) and transport anomaly time series of the first PEP (solid line). The transport time series of the PEP was calculated as in Figure 14.

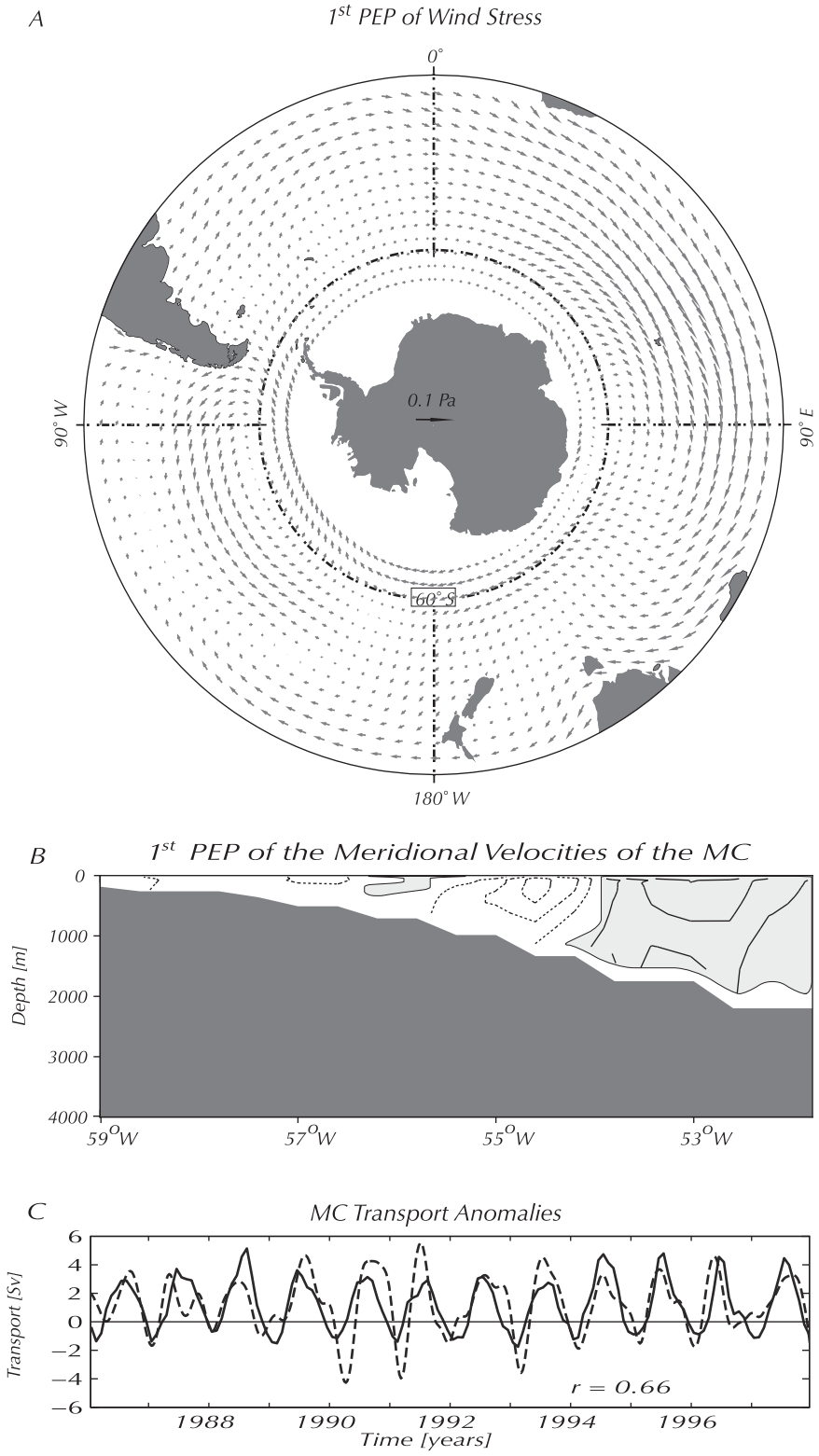

Figure 17. First PEP between the wind stress over the Southern Ocean and the meridional velocities of the Malvinas Current (Figure 1) showing (a) spatial amplitude of the wind stress, (b) spatial amplitude of the meridional velocities of the Malvinas Current (shaded is positive, 2 cm s^{-1} contour interval), and (c) transport anomaly time series from the model (dashed line) and transport anomaly time series of the first PEP (solid line). The transport time series of the PEP was calculated as in Figure 14.

South Pacific oceans are relatively smaller. The changes in the ACC velocity structure reflect meridional shifts of the various jets. The SAF and the PF abut during the winter and separate during the summer (Figure 16b). The spatial amplitudes of the ACC response to the wind stress and wind stress curl are characterized by the same patterns of variations of the SAF and the PF and by similar timescales (Figures 14b and 16b). Note that, to west of the Drake Passage, the atmospheric circulation associated with the wind stress anomalies in Figure 16a resembles the wind stress curl anomalies in Figure 14a. However, the correlation between the ACC transport and the time series of the first PEP with the wind stress is ~0.69 (the critical value at the 99% significance level is ~0.29), which is higher than the correlation between the ACC transport and the time series of the PEP with the wind stress curl (~0.56, the critical value at the 99% significance level is ~0.29). This indicates that the variability of the ACC transport is more strongly correlated with the variations of the wind stress in the latitudinal range of the Drake Passage than to those of the wind stress curl. Previous studies of the relation of the ACC transport to the wind suggest that the ACC is coherent with the wind stress in the latitudinal range of the Drake Passage and with the wind stress curl north of the Drake Passage [*Wearn and Baker*, 1980; *Gille et al.*, 2001; *Sprintall*, 2003]. The ACC response to the wind stress is mostly confined to the southern part of the Drake Passage where continuous contours of planetary potential vorticity provide a guide to the free propagation of these anomalies [*Hughes et al.*, 1999; *Gille et al.*, 2001; *Vivier et al.*, 2005].

[22] The first PEP of the MC accounts for approximately 40% of the total variability of the MC transport (Figure 17). It shows an offshore acceleration and an inshore deceleration of this current during the winter and a reversal toward the summer. Such patterns not only reflect absolute changes in the total transport of the MC, but also zonal displacements of its axis. The total transport of the MC reaches its maximum during September and its minimum during March. The wind stresses associated with these changes are characterized by an absolute maximum over the Southeastern Indian Ocean and absolute minimum over the South Atlantic. That is, this PEP indicates that the MC variability is more sensitive to the variations of the wind stress over the South Indian Ocean than to those on the South Atlantic Ocean. This result is consistent with the previous findings of *Vivier et al.* [2001], who reported that the winds over the Pacific-Indian sector have a stronger influence on the MC transport than those over the South Atlantic sector. It is interesting to note that, although the structure of velocity changes produced by the wind stress are very similar to those produced by the wind stress curl, the former accounts for a higher share of the MC variance than the latter, which is counterintuitive if one thinks of the MC as a western boundary current.

4. Conclusions

[23] In this article we investigated the origins of the variability of the MC in a global, eddy-permitting numerical simulation. It was shown that, although the model has a smaller level of kinetic energy than observations, it reproduces reasonably well some of the known characteristics of the low-frequency variabilities of the ACC and the MC transports. The analysis indicates that the observed low correlation between the transport variations of the ACC and the MC is due partly to the masking effect of high-frequency variability. We also showed the existence of a distinct mode, with a ~150-day period, that is generated at the Drake Passage and that propagates at speeds of ~6–7 cm s^{-1} toward the MC generating out-of-phase changes in the transport of the EB and the WB. These results were confirmed by the analysis of altimetry data. Our analysis also indicates that the ACC and the MC transports show positive transport anomalies during late winter and negative anomalies during late summer. The amplitude of the seasonal variations of the MC is only ~2 Sv, which is less than 4% of its mean transport. The seasonal amplitude is a little larger in the ACC (~3 Sv), but that represents less than 2% of its total transport. The small size of the seasonal variations in the ACC and MC transports, further masked by the high-frequency oscillations of the ACC, may explain why it has been difficult to find a statistically significant correlation between these two currents in observational data.

[24] The PEP analysis indicated that the dominant mode of covariability between the ACC and the wind forcing is associated with a maximum of the wind curl over the Pacific sector of the Southern Ocean. This mode causes an acceleration of the ACC during the winter and a deceleration during the summer. The most energetic timescales of variability of this mode are the annual, semiannual and an oscillation of ~150 days of period. Our analysis indicates that the increase of the ACC transport during the winter is characterized by an offshore acceleration and onshore deceleration of the Subantarctic Front that is followed by an offshore acceleration and onshore deceleration of the MC. During summer, these patterns are reversed in both currents. The wind stress curl anomalies forcing the MC are similar to those forcing the ACC: there is a maximum extending from the Drake Passage toward the Southeastern Indian sector of the Southern Ocean. The responses of the ACC and MC to the wind stress are qualitatively similar to those to the wind stress curl, but the wind stress accounts for slightly larger variances of the ACC and the MC transports. The wind stress PEPs of the ACC and MC show large wind stress anomalies over the South Indian Ocean extending toward midlatitudes. However, over the South Pacific Ocean, it is still possible to identify the same maxima of wind stress curl that were found in the PEPs computed with the wind stress curl.

Appendix A: Principal Estimator Pattern Decomposition

[25] When analyzing large amounts of information, a common problem in data analysis is to estimate spatial maps of some variable (the estimand) as a function of spatial maps of another variable (the estimator). The implicit hypothesis is that there is some sort of causal relationship between them, usually based on dynamical or empirical knowledge. The artificial skill of a linear statistical estimators is O(K/N*), where K is the number of data variables used to construct the estimator and N* is the effective number of degrees of freedom of the data. An effective way to reduce K, and hence the artificial skill of the

estimator, and at the same time maximize the variances of the estimand and estimator, is to represent both fields by their first few empirical orthogonal functions (EOF).

[26] Let the total estimator be estimated as a linear combination of the first M EOFs of the wind field, and the estimand be estimated as a linear combination of the first N EOFs of the vertical section of the velocity field, then, estimator and estimand can be approximated by:

$$\hat{W}(\vec{x},t)\sum_{m=1}^{M} w_m(t)W_m(\vec{x}) \tag{A1}$$

$$\hat{U}(\vec{y},t)=\sum_{n=1}^{N} u_n(t)U_n(\vec{y}) \tag{A2}$$

where $\hat{W}$ is the estimate of the wind field, $\hat{U}$ is the estimate of the velocity field, $\vec{x}$ and $\vec{y}$ (not necessarily coincident) are the spatial variables defining the grid locations and t represents time. The lowercase variables represent the amplitude time series of each mode, and the uppercase variables represent the spatial fields of each mode. The number of EOF modes (N and M) should be chosen such that they represent most of the variance of the original fields.

[27] One possibility for estimating the velocity at each section from the wind field would be to project the N orthogonal time series $u_n(t)$ onto the M orthogonal time series $w_m(t)$, and then write the former as a linear combination of the latter, formally:

$$\hat{u}_n(t)=\sum_{m=1}^{M}\alpha_{nm}w_m \tag{A3}$$

$$\alpha_{nm}=\frac{\langle u_n w_m\rangle}{\langle w_m^2\rangle} \tag{A4}$$

where the angle brackets represent the temporal mean. Because the EOF time series are uncorrelated with each other, the resulting fields could be interpreted as independent coupled modes of oscillation. The problem with this approach is that, if we have many EOFs, it is not easy to visualize the connections represented by the resulting fields.

[28] The goal of the PEP method is to look for a linear combination of a set of estimators (in this article, the first M EOFs of the wind stress or wind stress curl) that explains most of the variance of the estimand (in this article, the first N EOFs of the zonal velocities of the vertical section of the ACC, or the meridional velocities of the vertical section of the MC). The goal is to find a new orthonormal basis (z_m (t)) onto which to project the velocity field time series ($u_n(t)$), such that it maximizes the functional E:

$$w_n(t)=\sigma_n\sum_{m=1}^{M}\mu_{nm}z_m \tag{A5}$$

$$E=\sum_{n=1}^{N}\langle\hat{u}_n^2\rangle \tag{A6}$$

$$\sigma_n^2=\langle w_n^2\rangle \tag{A7}$$

where μ_{nm} are the elements of the rotation matrix. The maximization of (A6), after the substitution of (A3), (A4) and (A5) into (A6), using Lagrange multipliers, subject to the orthogonormality condition $\sum_k z_m(t_k)z_n(t_k)=\delta_{mn}$ ($\delta_{mn}=1$ if $m=n$ and $\delta_{mn}=0$ if $m\neq n$), yields the eigenvalue problem:

$$\sum_j A_{nj}\mu_{jm}-\lambda_m\mu_{nm}=0 \tag{A8}$$

$$A_{ij}=\sum_{n=1}^{N}\alpha_{ni}\alpha_{nj}\sigma_i\sigma_j. \tag{A9}$$

[29] After computing μ_{mm} and substituting it in (A5), the new orthonormal basis $z_m(t)$ can be found:

$$z_m(t)=\sum_{n=1}^{N}\mu_{nm}\frac{wn(t)}{\sigma_n}. \tag{A10}$$

[30] Using (A3)–(A5) it is possible to rewrite (A1) and (A2) as:

$$\hat{W}(\vec{x},t)=\sum_m z_m(t)Z_m(\vec{x}) \tag{A11}$$

$$\hat{U}(\vec{y},t)=\sum_m z_m(t)Q_m(\vec{y}) \tag{A12}$$

where:

$$Z_m(\vec{x})=\sum_n\sigma_n\mu_{nm}W_n(\vec{x}) \tag{A13}$$

$$Q_m(\vec{y})=\sum_{n=1}^{N}\sum_{m=1}^{M}\alpha_{nm}\sigma_m\mu_{mn}U_m(\vec{y}). \tag{A14}$$

[31] The field $Z_m(\vec{x})$ represents the spatial field of the m$^{\mathrm{th}}$ coupled mode of oscillation of the estimator (the wind field). The field $Q_m(\vec{y})$ represents the spatial field of the mth coupled mode of oscillation of the estimand (the velocity field). The expansion coefficients $Z_m(t)$ are the time series of the m$^{\mathrm{th}}$ coupled mode of variability between the estimator and the estimand.

[32] **Acknowledgments.** This paper greatly benefited from the criticism of two anonymous reviewers. The authors acknowledge the financial support of NSF grant OCE-0726994, NASA grants NAG512378 and NNX08AR40G, and JPL contract 1206714. Additional funding was provided by the Brazilian Research Council (CNPq) through grant 200825/98–4.

References

Agra, C., and D. Nof (1993), Collision and separation of boundary currents, *Deep Sea Res. Part I*, *40*, 2259–2282, doi:10.1016/0967-0637(93)90103-A.

Bracewell, R. N. (2003), *Fourier Analysis and Imaging*, 704 pp. Springer, New York.

Brandini, F. P., D. Boltovskoy, A. Piola, S. Kocnur, R. Rottgers, P. C. Abreu, and R. M. Lopes (2000), Multiannual trends in fronts and distribution of nutrients and chlorophyll in the southwestern Atlantic (30–62°S), *Deep Sea Res., Part I*, *47*, 1015–1033, doi:10.1016/S0967-0637(99)00075-8.

Chelton, D. B., and F. J. Wentz (2005), Global microwave satellite observations of sea surface temperature for numerical weather prediction and climate research, *Bull. Am. Meteorol. Soc.*, *86*(8), 1097–1115, doi:10.1175/BAMS-86-8-1097.

Cunningham, S. A., S. G. Alderson, and B. A. King (2003), Transport and variability of the Antarctic Circumpolar Current in Drake Passage, *J. Geophys. Res.*, *108*(C5), 8084, doi:10.1029/2001JC001147.

Davis, R. E. (1977), Techniques for statistical analysis and prediction of geophysical fluid systems, *Geophys. Astrophys. Fluid Dyn.*, *8*, 245–277, doi:10.1080/03091927708240383.

Davis, R. E. (1978), Predictability of sea level pressure anomalies over the North Pacific Ocean, *J. Phys. Oceanogr.*, *8*, 233–246, doi:10.1175/1520-0485(1978)008<0233:POSLPA>2.0.CO;2.

de Miranda, A. P., B. Barnier, and W. K. Dewar (1999), On the dynamics of the Zapiola Anticyclone, *J. Geophys. Res.*, *104*, 21,137–21,149, doi:10.1029/1999JC900042.

Ducet, N., P. Y. LeTraon, and G. Reverdin (2000), Global high resolution mapping of ocean circulation from the combination of TOPEX/Poseidon and ERS-1/2, *J. Geophys. Res.*, *105*, 19,477–19,498, doi:10.1029/2000JC900063.

Emery, W. J., and R. E. Thomson (2001), *Data Analysis Methods in Physical Oceanography*, 638 pp. Elsevier, Amsterdam.

Froneman, P. W., R. Perissinotto, and E. A. Pakhomov (1997), Biogeographical structure of the microphytoplancton assemblages in the region of the subtropical convergence and across a warm-core eddy during austral winter, *J. Plankton Res.*, *19*, 519–531, doi:10.1093/plankt/19.4.519.

Fu, L.-L. (2006), Pathways of eddies in the South Atlantic Ocean revealed from satellite altimeter observations, *Geophys. Res. Lett.*, *33*, L14610, doi:10.1029/2006GL026245.

Fu, L.-L. (2007), Interaction of mesoscale variability with large-scale waves in the Argentine Basin, *J. Phys. Oceanogr.*, *37*, 787–793, doi:10.1175/JPO2991.1.

Gan, J., L. A. Mysak, and D. N. Straub (1998), Simulation of the South Atlantic Ocean circulation and its seasonal variability, *J. Geophys. Res.*, *103*, 10,241–10,251, doi:10.1029/98JC00367.

Garzoli, S. L., and C. Giulivi (1994), What forces the variability of the southwestern Atlantic boundary currents?, *Deep Sea Res., Part I*, *41*, 1527–1550, doi:10.1016/0967-0637(94)90059-0.

Gille, S. T. (1997), The Southern Ocean momentum balance: Evidence for topographic effects from numerical model output and altimeter data, *J. Phys. Oceanogr.*, *27*, 2219–2232, doi:10.1175/1520-0485(1997)027<2219:TSOMBE>2.0.CO;2.

Gille, S. T., D. P. Stevens, R. T. Tokmakian, and K. J. Heywood (2001), Antarctic Circumpolar Current response to zonally averaged winds, *J. Geophys. Res.*, *106*, 2743–2759, doi:10.1029/1999JC900333.

Goni, G., S. Kamholz, S. Garzoli, and D. Olson (1996), Dynamics of the Brazil-Malvinas Confluence based on inverted echo sounders and altimetry, *J. Geophys. Res.*, *101*, 16,273–16,289, doi:10.1029/96JC01146.

Hofmann, E. E., and E. E. Whitworth III (1985), A synoptic description of the flow at Drake Passage from year-long measurements, *J. Geophys. Res.*, *90*, 7177–7187, doi:10.1029/JC090iC04p07177.

Hughes, C. W., M. P. Meredith, and K. J. Heywood (1999), Wind-driven transport fluctuations through Drake Passage: A southern mode, *J. Phys. Oceanogr.*, *29*, 1971–1992, doi:10.1175/1520-0485(1999)029<1971:WDTFTD>2.0.CO;2.

Inoue, M. (1982), Vertical structure of low-frequency currents at Drake Passage, Ph.D. dissertation, 220 pp., Tex. A&M Univ., College Station.

Johnson, G. C., and H. Bryden (1989), On the strength of the Circumpolar Current, *Deep Sea Res., Part A*, *36*, 39–53, doi:10.1016/0198-0149(89)90017-4.

Matano, R. P. (1993), On the separation of the Brazil Current from the coast, *J. Phys. Oceanogr.*, *23*, 79–90, doi:10.1175/1520-0485(1993)023<0079:OTSOTB>2.0.CO;2.

Matano, R. P., M. G. Shilax, and D. B. Chelton (1993), Seasonal variability in the southwestern Atlantic, *J. Geophys. Res.*, *98*, 18,027–18,035, doi:10.1029/93JC01602.

Meredith, M. P., P. L. Woodworth, C. W. Hughes, and V. Stepanov (2004), Changes in the ocean transport through Drake Passage during the 1980s and 1990s, forced by changes in the Southern Annular Mode, *Geophys. Res. Lett.*, *31*, L21305, doi:10.1029/2004GL021169.

Munk, W. H., and E. Palmén (1951), Note on the dynamics of the Antarctic Circumpolar Current, *Tellus*, *3*, 53–55.

Nowlin, W. D., Jr., and J. M. Klinck (1986), The physics of the Antarctic Circumpolar Current, *Rev. Geophys.*, *24*, 469–491, doi:10.1029/RG024i003p00469.

Olson, D. L., G. P. Podesta, R. H. Evans, and O. Brown (1988), Temporal variations in the separation of Brazil and Malvinas currents, *Deep Sea Res., Part A*, *35*, 1971–1990, doi:10.1016/0198-0149(88)90120-3.

Peterson, R. G. (1988), On the transport of the Antarctic Circumpolar Current through Drake Passage and its relation to wind, *J. Geophys. Res.*, *93*, 13,993–14,004, doi:10.1029/JC093iC11p13993.

Provost, C., O. Garcia, and V. Garçon (1992), Analysis of satellite sea surface temperature time series in the Brazil-Malvinas current confluence region: Dominance of the annual and semi-annual periods, *J. Geophys. Res.*, *97*, 17,841–17,858, doi:10.1029/92JC01693.

Smith, L. T., E. P. Chassignet, and D. B. Olson (1994), Wind-forced variations in the Brazil-Malvinas confluence region as simulated in a coarse-resolution numerical model of the South Atlantic, *J. Geophys. Res.*, *99*, 5095–5117, doi:10.1029/93JC03331.

Sprintall, J. (2003), Seasonal to interannual upper-ocean variability in the Drake Passage, *J. Mar. Res.*, *61*, 27–57, doi:10.1357/002224003321586408.

Stammer, D., R. Tokmakian, A. Sentner, and C. Wunsch (1996), How well does a $^1/_4°$ global circulation model simulate large-scale oceanic observations?, *J. Geophys. Res.*, *101*, 25,779–25,811, doi:10.1029/96JC01754.

Stommel, H. (1957), A survey of ocean current theory, *Deep Sea Res.*, *4*, 149–184.

Strub, P. T., C. James, A. C. Thomas, and M. R. Abbott (1990), Seasonal and nonseasonal variability of satellite-derived surface pigment concentration in the California Current, *J. Geophys. Res.*, *95*, 11,501–11,530, doi:10.1029/JC095iC07p11501.

Tansley, C. E., and D. P. Marshall (2001), On the dynamics of wind-driven circumpolar currents, *J. Phys. Oceanogr.*, *31*, 3258–3273, doi:10.1175/1520-0485(2001)031<3258:OTDOWD>2.0.CO;2.

Tokmakian, R., and P. G. Challenor (1999), On the joint estimation of model and satellite sea surface height anomaly errors, *Ocean Modell.*, *1*, 39–52, doi:10.1016/S1463-5003(99)00006-2.

Treguier, A. M., B. Barnier, A. P. de Miranda, J. M. Molines, N. Grima, M. Imbard, G. Madec, C. Messager, T. Reynaud, and S. Michel (2001), An eddy-permitting model of the Atlantic circulation: Evaluating open boundary conditions, *J. Geophys. Res.*, *106*, 22,115–22,130, doi:10.1029/2000JC000376.

Vivier, F., and C. Provost (1999), Volume transport of the Malvinas Current: Can the flow be monitored by TOPEX/Poseidon?, *J. Geophys. Res.*, *104*, 21,105–21,122, doi:10.1029/1999JC900056.

Vivier, F., C. Provost, and M. P. Meredith (2001), Remote and local forcing in the Brazil-Malvinas Region, *J. Phys. Oceanogr.*, *31*, 892–913, doi:10.1175/1520-0485(2001)031<0892:RALFIT>2.0.CO;2.

Vivier, F., K. A. Kelly, and M. Harismendy (2005), Causes of large-scale sea level variations in the Southern Ocean: Analyses of sea level and a barotropic model, *J. Geophys. Res.*, *110*, C09014, doi:10.1029/2004JC002773.

von Storch, H., and F. W. Zwiers (1999), *Statistical Analysis in Climate Research*, 484 pp. Cambridge Univ. Press, Cambridge, U.K.

Wainer, I., P. Gent, and G. Goni (2000), Annual cycle of the Brazil-Malvinas Confluence region in the National Center for Atmospheric Research Climate System Model, *J. Geophys. Res.*, *105*, 26,167–26,177, doi:10.1029/1999JC000134.

Wearn, R. B., Jr., and D. J. Baker (1980), Bottom pressure measurements across the Antarctic Circumpolar Current and their relation to the wind, *Deep Sea Res., Part A*, *27*, 875–888, doi:10.1016/0198-0149(80)90001-1.

Weijer, W., and S. T. Gille (2005), Adjustment of the Southern Ocean to wind forcing on synoptic timescales, *J. Phys. Oceanogr.*, *35*, 2076–2089, doi:10.1175/JPO2801.1.

A. F. H. Fetter and R. P. Matano, College of Oceanic and Atmospheric Sciences, Oregon State University, Corvallis, OR 97331-5503, USA. (tfetter@coas.oregonstate.edu)